Sub-10-nm Intracellular Bioelectronic Probes from Nanowire-Nanotube Heterostructures

Classification: PHYSICAL SCIENCES: Applied Physical Sciences and Applied Biological Sciences

Sub-10 nanometer intracellular bioelectronic probes from nanowire-nanotube heterostructures

Tian-Ming Fu[a], Xiaojie Duan[a,b,1], Zhe Jiang[a], Xiaochuan Dai[a], Ping Xie[a], Zengguang Cheng[a], and Charles M. Lieber[a,c,1]

[a]Department of Chemistry and Chemical Biology, Harvard University, Cambridge, Massachusetts, 02138, [b]Department of Biomedical Engineering, College of Engineering, Peking University, Beijing 100871, China, [c]School of Engineering and Applied Sciences, Harvard University, Cambridge, Massachusetts, 02138

Author Contributions: T.-M.F., XJ.D. (Xiaojie Duan), and C.M.L. designed research. T.-M.F., XJ.D., Z. J., and XC.D. (Xiaochuan Dai) performed experiments and analyses. T.-M.F., and P.X. performed theoretical modeling and simulation. Z.C. made the 3D figure. T.-M.F., XJ.D., and C.M.L. wrote the paper.

The authors declare no conflict of interest.

[1]To whom correspondence should be addressed. Tel: +86 10 6276 5681; E-mail: xjduan@pku.edu.cn (XJ.D) or Tel: +01 617 496 3169; Email: cml@cmliris.harvard.edu (C.M.L.).

This article contains supporting information.

Significance Statement

The miniaturization of bioelectronic probes to enable interrogation of small subcellular structures could impact significantly biology and medicine. This paper describes the design, fabrication and demonstration of the smallest bioelectronic devices realized to date by exploiting a unique three-dimension nanowire-nanotube structure, where a nanowire detector is synthetically-integrated with a nanotube probe. Devices with nanotube probe dimensions as small as 5 nm, which approach the size of a single ion channel, have been realized. Experimental measurements and numerical simulations show that these devices have sufficient time resolution to record the fastest electrical signals in neurons and other cells. Measurement of the cell transmembrane resting potential with these ultra-small bioelectronic devices further demonstrates their capability for intracellular electrophysiology studies.

Abstract: The miniaturization of bioelectronic intracellular probes with a wide dynamic frequency range can open up opportunities to study biological structures inaccessible by existing methods in a minimally invasive manner. Here, we report the design, fabrication and demonstration of intracellular bioelectronic devices with probe sizes less than 10 nm. The devices are based on a nanowire-nanotube heterostructure in which a nanowire field-effect transistor (FET) detector is synthetically-integrated with a nanotube cellular probe. Sub-10 nm nanotube probes were realized by a two-step selective etching approach that reduces the diameter of the nanotube free-end while maintaining a larger diameter at the nanowire detector necessary for mechanical strength and electrical sensitivity. Quasi-static water-gate measurements demonstrated selective device response to solution inside the nanotube, and pulsed measurements together with numerical simulations confirmed the capability to record fast

electrophysiological signals. Systematic studies of the probe bandwidth (BW) in different ionic concentration solutions revealed the underlying mechanism governing the time response. In addition, the BW effect of phospholipid coatings, which are important for intracellular recording, was investigated and modeled. The robustness of these sub-10 nm bioelectronics probes for intracellular interrogation was verified by optical imaging and recording the transmembrane resting potential of HL-1 cells. These ultra-small bioelectronic probes enable direct detection of cellular electrical activity with highest spatial resolution achieved to date, and with further integration into larger chip-arrays could provide a unique platform for ultrahigh resolution mapping of activity in neural networks and other systems.

Keywords: Nanoelectronics/ Field-effect transistor / Transmembrane potential recording/ Subcellular resolution/ Neural activity mapping

/body

Introduction

Intracellular electrical recording, which can reveal substantially greater details of cellular process compared with extracellular recording, is important for both biological studies and biomedical applications (1-8). Ideally, an intracellular probe should embody two essential characteristics: (*i*) it should be as small as possible to increase spatial resolution, which can provide access to small subcellular structures, and to reduce invasiveness; and (*ii*) it should have a sufficiently large frequency BW to record both fast signals related to opening/closing of ion channels (6, 9, 10) and slowly changing or DC signals associated with synaptic interactions (1, 2). Several approaches have been taken to achieve these goals (2, 11). Sharp microelectrodes, which access the cell interior by direct insertion of metal (1, 12) or carbon (13, 14) microelectrodes, and more recently chip-based arrays of vertical metal electrodes (11, 15-17), have been used to record intracellular and intracellular-like signals. Further development of these probes with respect to achieving the above miniaturization goals does, however, faces intrinsic limits related to increasing electrode impedance with decreasing size. The patch clamp micropipette technique also faces constraints for miniaturization related to increasing impedance with probe size reduction (2, 18).

An alternative approach that can overcome the above limitations of probe size reduction has focused on using active semiconductor nanowire FET detectors (7, 19, 20), which do not depend on interfacial impedance (21-23). The capability to control synthetically nanowire structure and morphology (24-31) also has enabled hierarchical design of several types of intracellular bioelectronic probes with sizes down to sub-100 nm regime (7, 19, 20). For example, branched intracellular nanotube field-effect transistors (BIT-FETs) (19), which are

designed based on a nanowire-nanotube heterostructure, achieve intracellular recording by penetrating the cell membrane with a silicon dioxide (SiO_2) nanotube thereby bringing the cell cytosol into contact with the underlying (extracellular) silicon nanowire (SiNW) FET detector.

Here we exploit the synthetic flexibility of this bioelectronic probe design to investigate reduction of the SiO_2 nanotube probe an order of magnitude to the sub-10 nm regime, which could open-up opportunities to interrogate small subcellular structures and organelles (Fig. 1*A*) and could provide high spatial resolution for mapping. To realize our sub-10 nm bioelectronic probe, there are three challenges that must be addressed. First, nanotube probes and their heterojunction with SiNW FETs will become mechanically less stable as diameter is reduced. Second, the electrical sensitivity will be reduced with decreasing nanotube diameter since the nanotube inner diameter (ID) defines the effective device gate area. Third, high frequency dynamic response may degrade with decreasing nanotube ID due to increasing solution resistance in the nanotube. Our synthesis, fabrication, and characterization studies described below show how these challenges can be successfully met to realize a functional sub-10 nm bioelectronic probe.

Results and Discussion

Our target for the ultra-small BIT-FET incorporating a sub-10 nm nanotube probe (Fig. 1*A* and *B*) has several key features to enable sufficient mechanical strength and electrical sensitivity as follows. First, the nanotube probe has a long free-end with small ID and thin wall for facile and minimally-invasive cell penetration. Second, a much larger ID and thicker wall are used for the bottom part of the nanotube to provide mechanical stability and increase the effective gate area

of the SiNW FET detector. This latter feature can also ensure high electrical sensitivity of the bioelectronic probe.

To realize this target device structure we developed an efficient multi-step synthesis and fabrication approach (Fig. 1*C*; Figs. S1 and S2; *SI Text*). First, SiNW FETs were fabricated on a substrate surface (Fig. S1 *A* and *B*) using previously established methods (25). Second, germanium nanowire (GeNW) branches, which serve as sacrificial templates for the nanotube probes (19), were grown on top of the SiNW FETs via our gold-nanoparticle catalyzed method (26) with the nanoparticle position precisely defined by electron beam lithography between the source and drain (S/D) electrodes of the FET (Fig. S1 *C* and *D*). A representative scanning electron microscopy (SEM) image shows a nearly vertical GeNW grown from the upper surface of the SiNW (Fig. 1*C, I*). Third, selective hydrogen peroxide (H_2O_2) etching was carried out to reduce the size of the upper portions of the GeNWs while the lower portions of the GeNWs where they connect to the SiNWs are protected by a thin photoresist layer with thickness about 20% of the entire GeNW length (Fig. S1 *E* and *F*). A typical SEM image (Fig. 1*C, II*) shows that this selective etching step yields GeNWs with diameters <10 nm for the upper portions and diameters ca. 80-90 nm for the lower portions. The larger diameter for the lower portion enhances the mechanical strength of the structure, and together with the Ge shell deposited on the SiNW (simultaneously with GeNW growth), is also important to the overall device sensitivity as discussed below.

To form the nanotube structure, a thin ca. 30 nm SiO_2 layer was conformally deposited by atomic layer deposition (ALD) on the SiNW-branched GeNW heterostructures and entire device substrate (Fig. S1*G*; Fig. S2*A*). In addition to coating the GeNW, this ALD process deposits the same thickness SiO_2 on the SiNW FET and S/D electrodes, and thus serves to

passivate (i.e., isolate) these structures from solution in our experiments. Selective buffered hydrofluoric acid (BHF) etching was then carried out to reduce the thickness of upper SiO_2 shell to ~10 nm while the lower portion of the shell was protected by photoresist (Fig. S1 *H* and *I*; Fig. S2*A*). To complete the device structure, a two-step etching process was carried out in a manner similar to that described previously for the conventional BIT-FET (20). First, the upper tip of the Ge core was exposed by removing the SiO_2 shell using BHF, and then the GeNW was removed using H_2O_2. A representative SEM image of an ultra-small BIT-FET (Fig. 1*C*, *III*) shows several key features. First, the upper portion of the SiO_2 nanotube has an ID of ~8 nm and a wall thickness of ~10 nm thick. Second, the very tip of the nanotube is tapered due to BHF etching yielding a relative sharp point for insertion. Third, the lower portion of the nanotube has much larger ~80 nm ID and 30 nm wall thickness as expected based on our fabrication process. In addition, transmission electron microscopy (TEM) images (Fig. S2*B*) confirm the ultrasmall IDs of the upper portions of the SiO_2 nanotubes.

The basic electrical sensitivity of the ultra-small BIT-FET devices before and after GeNW etching was characterized using standard quasi-static water-gate measurements (19, 32) (see *SI Text*). Representative device conductance, G, versus applied water-gate voltage, V_{wg}, data (Fig. 2*A*) shows that G changes very little as a function of V_{wg} before GeNW etching, but exhibits a large change after GeNW etching to form the nanotube structure. Indeed, the magnitude of the transconductance (device sensitivity) increases from 0.24 to 2.75 μS/V after etching. In addition, control measurements performed on SiNW FET devices without nanotubes or GeNW branches exhibit no increase in transconductance after etching similar to previous studies (19). Together, these results confirm that solution can fill a small SiO_2 nanotubes, and

that the SiNW FET detector responds selectively to the solution inside the nanotubes versus outside.

The enhanced sensitivity following GeNW etching to form the nanotube probe structure reflects two key contributions. First, the solution gating the SiNW FET via a much thinner (1-2 nm native oxide) SiO_2 versus 30 nm deposited layer before GeNW etching. Second, the Ge-layer deposited on the SiNW FET during GeNW growth is etched during nanotube formation process to yield an effective gate area that is much larger than that defined by the nanotube ID (Fig. 1*B*; Fig. S3).

We characterized the bandwidth (BW) of the ultra-small BIT-FETs through step water-gate pulse measurements in 1x phosphate buffered saline (1x PBS) solution (see *SI Text*) to define further their capabilities for electrophysiological recording in cells. The temporal response of a device with 10 nm ID nanotube following a step-like water-gate pulse (rise time = 0.01 msec, amplitude = 100 mV) is shown in Fig. 2*B*, where the capacitive coupling from the metal contacts was removed (Fig. S4) and the measured conductance change was converted to voltage using the device sensitivity (32). Qualitatively, the recorded data exhibits a slower time response (i.e., rounding with respect to water-gate voltage step), which indicates that the probe's time response is slower than 0.01 msec rise time of the applied voltage step. Following previous studies (19), we can define the effective BW as,

$$BW = \frac{0.35}{t_{90\%} - t_{10\%}} \quad (1)$$

where $t_{90\%} - t_{10\%}$ is the time needed for the recorded signal to change from 10% to 90% of the steady-state amplitude of the applied V_{wg}. Analysis of the data in Fig. 2*B*, where $t_{90\%}$ - $t_{10\%}$ = 58 μs, yield a BW of ~ 6.0 kHz.

To further elucidate the nanotube ID dependence of the ultra-small BIT-FETs BW, we carried out similar pulsed water-gate measurements for ultra-small BIT-FET devices with different nanotube IDs. The measured calibrated voltage signal as a function of time data for devices with nanotube IDs from 5 to 22 nm (Fig. 2*C*) show that the rise time for the recorded signal to reach 100 mV steady-state increases as the nanotube ID decreases. Quantitatively, the calculated BW of each probe based on equation (1) are shown in Fig. 2*D*. These data show that BW decreases from ca. 88 kHz to 3.1 kHz as the nanotube ID decreases from (22 to 5 nm, respectively.

To gain further insight into the measured data we also modeled the ultra-small BIT-FET BW (Fig. S5*A*). The time evolution of the potential at the SiNW FET surface following a step-like pulsed water-gate potential was numerically evaluated (see *SI Text*) for two different models. The upper BW limit (Model 1) assumes the active gate area is defined by the nanotube ID (e.g., Fig. S3*A*), and the lower BW limit (Model 2) assumes that the entire SiNW surface is active (i.e., the deposited Ge layer is etched over the SiNW surface as shown schematically in Fig. S3*B*). The calculated BW results for the two models (Fig. 2*D*) are consistent with the experimental data, although somewhat overestimates BW at the smaller diameters. This difference can be attributed to a larger gap over the SiNW FET detector (Fig. S3*B*) than used in Model 2, although future studies will be required to understand fully these differences. Importantly, we note that the measured and calculated BW values for the smallest 5 nm ID nanotube probes, 3.1 kHz, are sufficient to enable accurate recording of most fast dynamic cellular processes.

We have further characterized the BW of the ultra-small BIT-FETs in different ionic strength PBS solutions. Representative data recorded following a water-gate potential step using an ultra-small BIT-FET with 10 nm ID nanotube (Fig. 3*A*) exhibit a clear increase of rise time

with decreasing solution concentration. A plot of the BW versus solution concentration determined from this data (Fig. 3*B*) shows that the BW depends linearly on PBS concentration. Qualitatively, this behavior is consistent with our model given the expected dependence of BW on solution resistivity.

We have further explored this dependence by recording the time response from ultra-small BIT-FETs with different nanotube IDs in different concentration PBS solutions, where the resulting BW results are summarized in Fig. 3*C*. In addition, these results were rescaled by normalizing the solution resistivity to that in 1x PBS (Fig. 3*D*); that is, multiplying the BW by $\rho_{sol}/\rho_{1x\ PBS}$, where ρ_{sol} and $\rho_{1x\ PBS}$ are the resistivity of the solution and 1x PBS solution, respectively. The rescaled data exhibits a nearly universal dependence on nantube ID, where we attribute deviations to contributions from the tip access impedance and capacitive coupling to the underlying SiNW FET. These latter factors become more prominent for larger ID nanotube devices, although we assume that the BW is dominated only by the nanotube in our analysis. We have also used a simplified analytical model to obtain additional insight into the device behavior (*SI Text*). Specifically, this analysis provides an explicit relationship for the BW as a function of solution resistivity inside the nanotube (inverse), the nanotube wall capacitance per unit length (inverse) and nanotube length (inverse square root), and thus also can be used to guide the design of ultra-small BIT-FETs to achieve required BWs.

The ultra-small BIT-FET nanotubes are coated with phospholipid layers to facilitate the cell membrane penetration for intracellular recording (7, 19, 20, 33-36). Because the smallest nanotube IDs investigated in our studies approach the thickness of phospholipid bilayer ~ 4.75 nm (37), we measured the BWs of several probes before and after phospholipid modification (*Materials and Methods*). Analysis of data recorded with an ultra-small BIT-FET having a 10

nm ID and 2.8 μm long nanotube (Fig. 4*A*) shows that the BW dropped from 9.7 kHz to 3.0 kHz after phospholipid modification while the device sensitivity remained essentially unchanged (< 1% variation in transconductance).

To explain the observed reduction in BW in this and other measurements following phospholipid modification, we considered the three scenarios shown schematically in Fig. 4*B*: (*i*) the entire inner and outer nanotube surfaces of the nanotube are covered by a lipid bilayer; (*ii*) a phospholipid bilayer covers 50% of the inner and all of the outer surfaces of the nanotube; (*iii*) the lipid bilayer is excluded from the inner surface but covers all of the outer surface of the nanotube. The calculated (*SI Text*) BW change expressed as a ratio after:before phospholipid modification for these three scenarios as a function of nanotube ID (Fig. 4*C*) highlights several key points. First, the BW ratio approaches zero for case-*i* and case-*ii* as the nanotube ID approaches the thickness of the bilayer coatings due to the increasing effective solution resistivity. Second and for case-*iii*, the ratio is >1 due to a reduction in effective capacitance of the nanotube. In addition, comparison of these calculations to experimental results for 15 and 10 nm ID nanotube probes (Fig. 4*C*) shows that the experimental BW ratios are close to case-*i* and case-*ii*, respectively. In the future, systematic experimental studies should give insight to the control of phospholipid modification to minimize coating of the inner nanotube wall while maintaining coverage of the outer surface to facilitate probe penetration through cell membranes, although we note that the BW drops on modification still yield sufficiently high BWs for 10 nm ID nanotubes to record sub-millisecond cellular processes such as neuronal action potentials (2, 3, 11).

Last, we have investigated the capability of the ultra-small BIT-FET for intracellular recording in studies of isolated HL-1 cells (38). A series of differential interference contrast

optical microscopy images recorded while moving a single HL-1 cell with a glass micropipette to/from a phospholipid modified ultra-small BIT-FET with 10 nm ID nanotube probe (Fig. 5*A*) shows several features. First, the substantial size difference between the ultra-small BIT-FET and glass micropipette is obvious in the images. Second, the nanotube probe can readily penetrate the cell membrane without affecting the overall cell shape, which suggests a biomimetic internalization assisted by lipid modification and hence a reasonably tight seal around the nanotube. Third, when the cell is retracted from the nanotube probe there is no change in cell shape indicating that the membrane readily reseals.

Significantly, measurement of the potential (mV) during the HL-1 cell approach/penetration/retraction process with an independent ultra-small BIT-FET (Fig. 5*B*) shows (*i*) a stable baseline prior to contact, (*ii*) a sharp ca. 59 mV drop when the HL-1 cell was brought into contact with the ultra-small nanotube, which corresponds to the intracellular potential of the cell, and (*iii*) abrupt (within ~300 ms) return to baseline coincident with retraction of the HL-1 cell from the device. These data demonstrate that the ultra-small BIT-FET can record intracellular potentials, and moreover, can record both low frequency (shown here) and high-frequency (described above) signals. The capability to record signals over a broad frequency range using 10 nm scale probe represents a clear advantage of the active ultra-small BIT-FET device over conventional passive electrodes.

Conclusions

We have designed, fabricated and demonstrated an ultra-small intracellular bioelectronic probe, the ultra-small BIT-FET, based on a nanowire-nanotube heterostructure with probe nanotubes having IDs as small as 5 nm. Systematic studies of the ultra-small BIT-FET BW through pulsed

water-gate measurements and theoretical modeling showed the capability to record fast, sub-millisecond physiological signals with the smallest ID nanotube probes. Moreover, the effect of phospholipid coatings, which are important for intracellular recording, on probe performance has been characterized and modeled. Importantly, optical microscopy and electrical recording measurements demonstrate that ultra-small BIT-FET nanotube probes can penetrate and subsequently be retracted from HL-1 cells in minimally-invasive manner while continuously recording the transition between extracellular and intracellular rest potential. The ultra-small BIT-FET opens up unique opportunities for future electrophysiological researches, including intracellular recordings from small subcellular structures and intracellular organelles, such as dendrites, dendritic spines, and the cell nucleus. Integration of such probes into large-scale arrays could also enable mapping of electrical activity from neural networks with substantially greater spatial resolution and minimal invasiveness than possible with techniques now available.

Materials and Methods

Nanowire Synthesis and device fabrication. Key steps in nanowire synthesis and device fabrication are described in *SI Text* and Fig. S1. First, single-crystalline SiNWs were synthesized using the Au nanocluster-catalyzed vapor-liquid-solid growth methodology in a home-built chemical vapor deposition (CVD) system (17). Second, SiNW FETs were fabricated on Si_3N_4 covered Si wafers. Third, GeNWs were grown on top of SiNW FETs using the same CVD system, and the upper portions of the GeNWs were etched in hydrogen peroxide (H_2O_2) solution to reduce their diameters to the 10 nm regime. Fourth, a 30 nm thick SiO_2 layer was conformally deposited by ALD and then selective BHF etching was used to reduce the upper portion of the

SiO_2 layer down to ca. 10 nm thickness. Finally, the tip SiO_2 was removed by BHF and the GeNW core was removed by H_2O_2 etching to form the nanotube probe.

Device characterization. Two types of water-gate characterization measurements were carried out to elucidate the behavior of the ultra-small BIT-FET in aqueous solution: (*i*). Standard quasi-static water-gate measurements were made in 1x PBS to determine device sensitivity. (*ii*). A step-like pulsed water-gate measurement was used to characterize the bandwidth (BW) of the ultra-small BIT-FET in different concentration PBS solutions. The details of each measurement are described in *SI Text*.

Phospholipid modification. SiO_2 nanotubes with negatively charged surfaces were incubated with lipid vesicles of 1,2-dimyristoyl-snglycero-3-phosphocholine (DMPC, Avanti Polar Lipids Inc.) containing 1% 1-myristoy1-2-{12-[(7-nitro-2-1,3-benzoxadiazol-4-yl)] amino dodecanoyl}-sn-glycero-3-phosphocholine (NBD-lipid, Avanti Polar Lipids Inc.) as fluorescent reporter to form supported lipid layers. The detailed procedure for this modification process was described in previous literature (7, 36). Fluorescence microscopy images of dye-labeled DMPC modified ultra-small BIT-FETs were carried out each time after modification to ensure the lipid bilayers form a continuous shell on the SiO_2 nanotube.

Cell recordings. HL-1 cell culture and phospholipid modification of device chips were carried out following reported methods (7, 19). Trans-membrane recording and cell manipulation were carried out in Tyrode solution (pH ~7.3) with a 100 mV DC source voltage at 37°C. The

recording current was amplified with a home-built multi-channel current/voltage preamplifier, filtered with a 500 Hz low pass filter (CyberAmp 380), and digitized at a 50 kHz sampling rate (Axon Digi1440A). Ag/AgCl electrodes were used to fix the extracellular solution potential.

Acknowledgments

The authors thank M. Mankin for assistance in TEM imaging and H. S. Choe, J. Liu, C. Xie, R. Gao, R. Day, and J. Huang for helpful discussions. XJ.D. acknowledges the support from the National Natural Science Foundation of China (No. 21373013), and the National Basic Research Program of China (No. 2014CB932500). C.M.L. acknowledges support of this research from DOD NSSEFF (N00244-09-1-0078) Award.

References

1. Purves RD (1981) *Microelectrode methods for intracellular recording and ionophoresis* (Academic Press, London ; New York) pp x, 146 p.
2. Molleman A (2003) *Patch clamping : an introductory guide to patch clamp electrophysiology* (J. Wiley, New York) pp x, 175 p.
3. Erickson J, Tooker A, Tai YC, & Pine J (2008) Caged neuron MEA: a system for long-term investigation of cultured neural network connectivity. *Journal of neuroscience methods* 175(1):1-16.
4. Voelker M & Fromherz P (2005) Signal transmission from individual mammalian nerve cell to field-effect transistor. *Small* 1(2):206-210.
5. Hille B (2001) *Ion channels of excitable membranes* (Sinauer, Sunderland, Mass.) 3rd Ed pp xviii, 814 p.

6. Dunlop J, Bowlby M, Peri R, Vasilyev D, & Arias R (2008) High-throughput electrophysiology: an emerging paradigm for ion-channel screening and physiology. *Nat Rev Drug Discov* 7(4):358-368.

7. Tian BZ, *et al.* (2010) Three-Dimensional, Flexible Nanoscale Field-Effect Transistors as Localized Bioprobes. *Science* 329(5993):830-834.

8. Duan XJ, Fu TM, Liu J, & Lieber CM (2013) Nanoelectronics-biology frontier: From nanoscopic probes for action potential recording in live cells to three-dimensional cyborg tissues. *Nano today* 8(4):351-373.

9. Meyer T, Boven KH, Gunther E, & Fejtl M (2004) Micro-electrode arrays in cardiac safety pharmacology: a novel tool to study QT interval prolongation. *Drug safety : an international journal of medical toxicology and drug experience* 27(11):763-772.

10. Zheng W, Spencer RH, & Kiss L (2004) High throughput assay technologies for ion channel drug discovery. *Assay and drug development technologies* 2(5):543-552.

11. Spira ME & Hai A (2013) Multi-electrode array technologies for neuroscience and cardiology. *Nat Nanotechnol* 8(2):83-94.

12. Hubel DH (1957) Tungsten Microelectrode for Recording from Single Units. *Science* 125(3247):549-550.

13. Schrlau MG, Dun NJ, & Bau HH (2009) Cell electrophysiology with carbon nanopipettes. *ACS nano* 3(3):563-568.

14. de Asis ED, Jr., Leung J, Wood S, & Nguyen CV (2010) Empirical study of unipolar and bipolar configurations using high resolution single multi-walled carbon nanotube electrodes for electrophysiological probing of electrically excitable cells. *Nanotechnology* 21(12):125101.

15. Robinson JT, *et al.* (2012) Vertical nanowire electrode arrays as a scalable platform for intracellular interfacing to neuronal circuits. *Nat Nanotechnol* 7(3):180-184.

16. Xie C, Lin ZL, Hanson L, Cui Y, & Cui BX (2012) Intracellular recording of action potentials by nanopillar electroporation. *Nat Nanotechnol* 7(3):185-190.

17. Hai A, *et al.* (2009) Changing gears from chemical adhesion of cells to flat substrata toward engulfment of micro-protrusions by active mechanisms. *Journal of neural engineering* 6(6):066009.

18. Sakmann B & Neher E (1984) Patch clamp techniques for studying ionic channels in excitable membranes. *Annual review of physiology* 46:455-472.

19. Duan XJ, *et al.* (2012) Intracellular recordings of action potentials by an extracellular nanoscale field-effect transistor. *Nat Nanotechnol* 7(3):174-179.

20. Gao RX, *et al.* (2012) Outside Looking In: Nanotube Transistor Intracellular Sensors. *Nano Lett* 12(6):3329-3333.

21. Sze SM (1982) Citation Classic - Physics of Semiconductor-Devices. *Cc/Eng Tech Appl Sci* (27):28-28.

22. Patolsky F, Zheng GF, & Lieber CM (2006) Nanowire-based biosensors. *Anal Chem* 78(13):4260-4269.

23. Misra N, *et al.* (2009) Bioelectronic silicon nanowire devices using functional membrane proteins. *Proc Natl Acad Sci U S A* 106(33):13780-13784.

24. Morales AM & Lieber CM (1998) A laser ablation method for the synthesis of crystalline semiconductor nanowires. *Science* 279(5348):208-211.

25. Cui Y, Wei QQ, Park HK, & Lieber CM (2001) Nanowire nanosensors for highly sensitive and selective detection of biological and chemical species. *Science* 293(5533):1289-1292.

26. Lauhon LJ, Gudiksen MS, Wang CL, & Lieber CM (2002) Epitaxial core-shell and core-multishell nanowire heterostructures. *Nature* 420(6911):57-61.

27. Wu Y, Xiang J, Yang C, Lu W, & Lieber CM (2004) Single-crystal metallic nanowires and metal/semiconductor nanowire heterostructures (vol 430, pg 61, 2004). *Nature* 430(7000):704-704.

28. Yang C, Zhong ZH, & Lieber CM (2005) Encoding electronic properties by synthesis of axial modulation-doped silicon nanowires. *Science* 310(5752):1304-1307.

29. Lu W, Xiang J, Timko BP, Wu Y, & Lieber CM (2005) One-dimensional hole gas in germanium/silicon nanowire heterostructures. *P Natl Acad Sci USA* 102(29):10046-10051.

30. Tian BZ, *et al.* (2007) Coaxial silicon nanowires as solar cells and nanoelectronic power sources. *Nature* 449(7164):885-U888.

31. Kempa TJ, *et al.* (2012) Coaxial multishell nanowires with high-quality electronic interfaces and tunable optical cavities for ultrathin photovoltaics. *P Natl Acad Sci USA* 109(5):1407-1412.

32. Patolsky F, Zheng GF, & Lieber CM (2006) Fabrication of silicon nanowire devices for ultrasensitive, label-free, real-time detection of biological and chemical species. *Nat Protoc* 1(4):1711-1724.

33. Chernomordik LV & Kozlov MM (2008) Mechanics of membrane fusion. *Nat Struct Mol Biol* 15(7):675-683.

34. VanDersarl JJ, Xu AM, & Melosh NA (2012) Nanostraws for direct fluidic intracellular access. *Nano Lett* 12(8):3881-3886.

35. Almquist BD & Melosh NA (2010) Fusion of biomimetic stealth probes into lipid bilayer cores. *Proc Natl Acad Sci U S A* 107(13):5815-5820.

36. Huang SC, *et al.* (2007) Formation, stability, and mobility of one-dimensional lipid bilayers on polysilicon nanowires. *Nano Lett* 7(11):3355-3359.

37. Stern HA & Feller SE (2003) Calculation of the dielectric permittivity profile for a nonuniform system: Application to a lipid bilayer simulation. *J Chem Phys* 118(7):3401-3412.

38. Claycomb WC, *et al.* (1998) HL-1 cells: A cardiac muscle cell line that contracts and retains phenotypic characteristics of the adult cardiomyocyte. *P Natl Acad Sci USA* 95(6):2979-2984.

Figure Legends

Fig. 1. Schematics and scanning electron microscopy (SEM) images of the ultra-small BIT-FET. (*A*) Schematic illustration of an intracellular bioelectronic probe. *Left panel*: General scheme of a probe for intracellular electrophysiology recording. *Right panel*: A magnified view of the tip of a sub-10 nm bioelectronic probe and its related size to single ion channel. (*B*) Schematic structure of the ultra-small BIT-FET. Green, yellow, blue and grey colors represent SiO_2 layer, metal contact, SiNW and silicon nitride substrate, respectively. (*C*) SEM images of the ultra-small BIT-FET at different fabrication steps. A GeNW branch was first grown on top of SiNW (*I*), followed by a subsequent H_2O_2 etching of top part of GeNW to shrink its diameter

down to sub-10 nm regime (*II*). A final view of an ultra-small BIT-FET with nanotube ID ~8 nm, and SiO_2 wall thickness ~10 nm is presented in (*III*). Top inset of *III* is the close-up image of the tip of the ultra-small SiO_2 nanotube. White dashed lines in *II* and *III* indicate the point below which the GeNW and SiO_2 is protected by photoresist during H_2O_2 and BHF etching, respectively. All scale bars are 100 nm.

Fig. 2. Water-gate characterization and bandwidth (BW) measurements. (*A*) Conductance *G* of an ultra-small BIT-FET with ~7 nm ID versus water-gate voltage V_{wg} before (blue) and after (red) core GeNW etching. (*B*) A step water-gate pulse V_{wg} with 0.01 ms rise time and 100 mV steady-state amplitude (black) and the corresponding response from a typical ultra-small BIT-FET with ~10 nm nanotube ID and 3.2 μm length (red). Response from metal contacts has been removed (Fig. S4). The recorded voltage signal is calibrated by the device transconductance measured from quasi-static water-gate experiment. V_{wg} and V_{signal} are offset by 50 mV for clarity. (*C*) Step pulsed water-gate responses from ultra-small BIT-FETs with different nanotube IDs. Same voltage calibration was adopted as (*B*). Traces are offset by 100 mV for clarity. (*D*) Measured BW of ultra-small BIT-FET devices versus the ID of the nanotube and comparison with numerically calculated data. Model 1 and 2 present the upper (the active gate area is defined by the nanotube ID) and the lower limit (the entire SiNW surface is active) of the device (*SI Text*). For comparison, all the BWs were normalized to a uniform nanotube length of 2.5 μm. Due to the equipment BW limit, the BW of the 22 nm device is extrapolated from its BW in 0.1x PBS solution by taking the relative conductivity of 1x PBS and 0.1x PBS into account (*SI Text*). The error bar corresponding to the standard error of the experimental data is ±

2 nm induced by SEM measurement uncertainty. All the devices for experiment and modeling have a top nanotube wall thickness ~10 nm.

Fig. 3. Device bandwidth dependence on electrolyte concentration. (*A*), (*B*) Pulsed water-gate responses (traces offset by 100 mV) and corresponding BWs of a ~10 nm nanotube ID ultra-small BIT-FET in solutions with different PBS concentration. (*C*) Measured BWs of ultra-small BIT-FET devices versus nanotube ID in different concentration PBS solutions. (*D*) Rescaled device BWs versus nanotube ID. All BWs are rescaled by solution resistivity (*SI Text*).

Fig. 4. Device bandwidth after phospholipid modification. (*A*) Pulsed water-gate responses from a ~10 nm nanotube ID ultra-small BIT-FET before (black) and after (red) phospholipid modification. The black and red arrows indicate the points when the curves reach steady-state amplitudes. Traces are offset by 100 mV for clarity. (*B*) Schematics of three possible scenarios for phospholipid modification: both (inner and outer) surfaces of the nanotube are fully covered (*left*), outer surface is fully covered and inner surface is only 50% covered (*middle*) and only outer surface is covered (*right*). The purple and green colors are phospholipid bilayer and SiO_2 nanotube, respectively. (*C*) Calculated ratio of the device BW after and before phospholipid modification versus nanotube ID under different scenarios depicted in (*A*) (*SI Text*). For comparison, two experimental data are presented (black square).

Fig. 5. Intracellular resting membrane potential recording. (*A*) Schematics (*upper panel*) and differential interference contrast optical microscopy images (*lower panel*) of an HL-1 cell manipulated by a glass micropipette to approach (*I*), contact (*II*), penetrate (*III*), and retract (*IV*)

from a phospholipid-modified ultra-small BIT-FET probe. Red arrow indicates the position of the ultra-small nanotube tip. Since pure SiO_2 nanotube is optically-transparent, the GeNW template of this device was not etched for imaging. Scale bar: 2 μm. (*B*) Representative electrical recording results from a ~10 nm ID ultra-small BIT-FET device; in this case, the GeNW was etched to yield the ultra-small SiO_2 nanotube. Down and up pointing green arrows mark the beginning of cell penetration and withdrawal, respectively. The upper and lower horizontal dashed line indicate the extracellular and intracellular potentials. Quasi-static water-gate measurements made before/after cell measurements show <2% change in the device conductance and sensitivity.

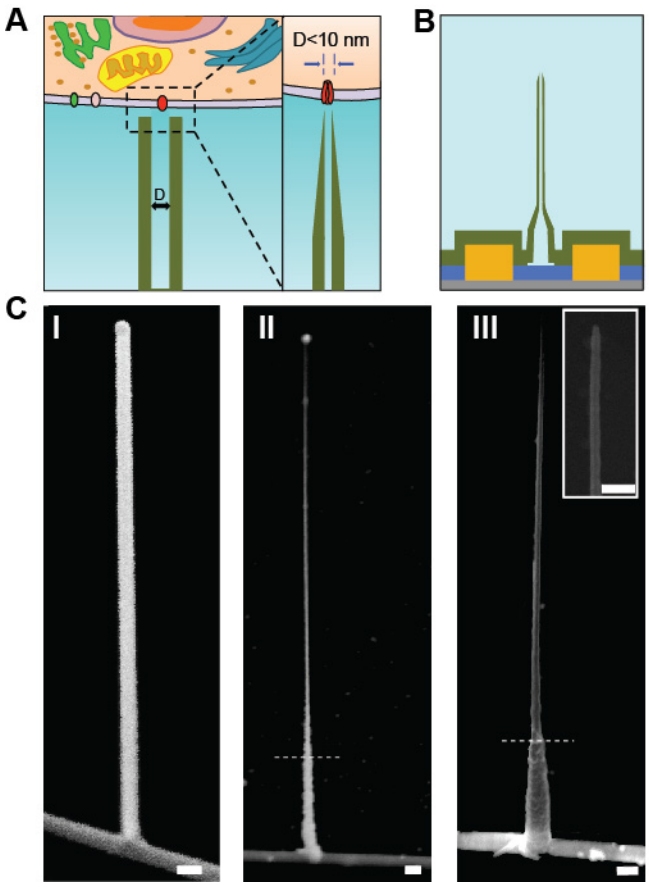

Figure 1

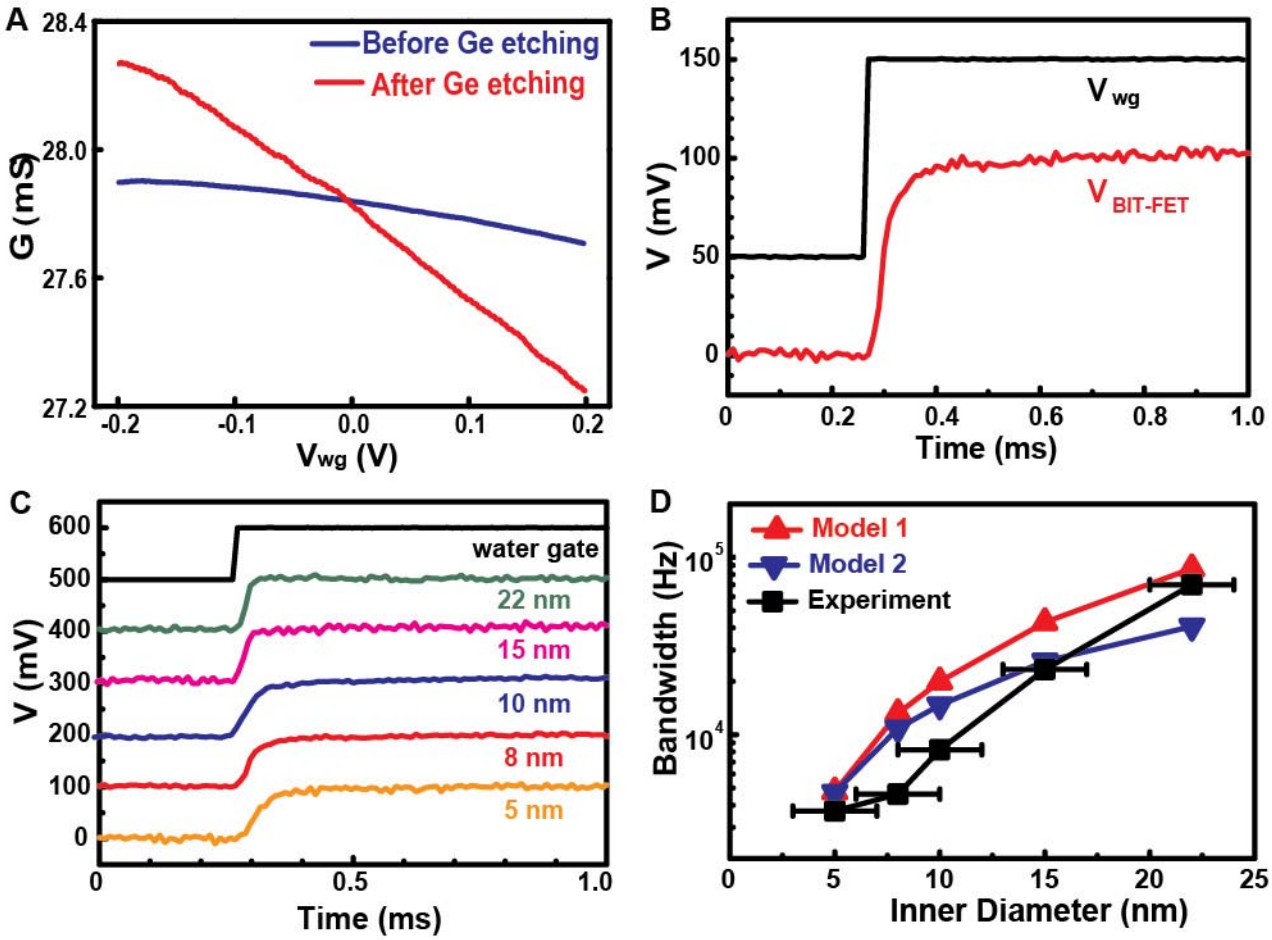
A
Before Ge etching
After Ge etching
G (mS)
28.4
28.0
27.6
27.2
-0.2
-0.1
0.0
0.1
0.2
Vwg (V)
B
Vwg
VBIT-FET
V (mV)
150
100
50
0
0
0.2
0.4
0.6
0.8
1.0
Time (ms)
C
water gate
22 nm
15 nm
10 nm
8 nm
5 nm
V (mV)
600
500
400
300
200
100
0
0
0.5
1.0
Time (ms)
D
Model 1
Model 2
Experiment
Bandwidth (Hz)
10^5
10^4
0
5
10
15
20
25
Inner Diameter (nm)

Figure 2

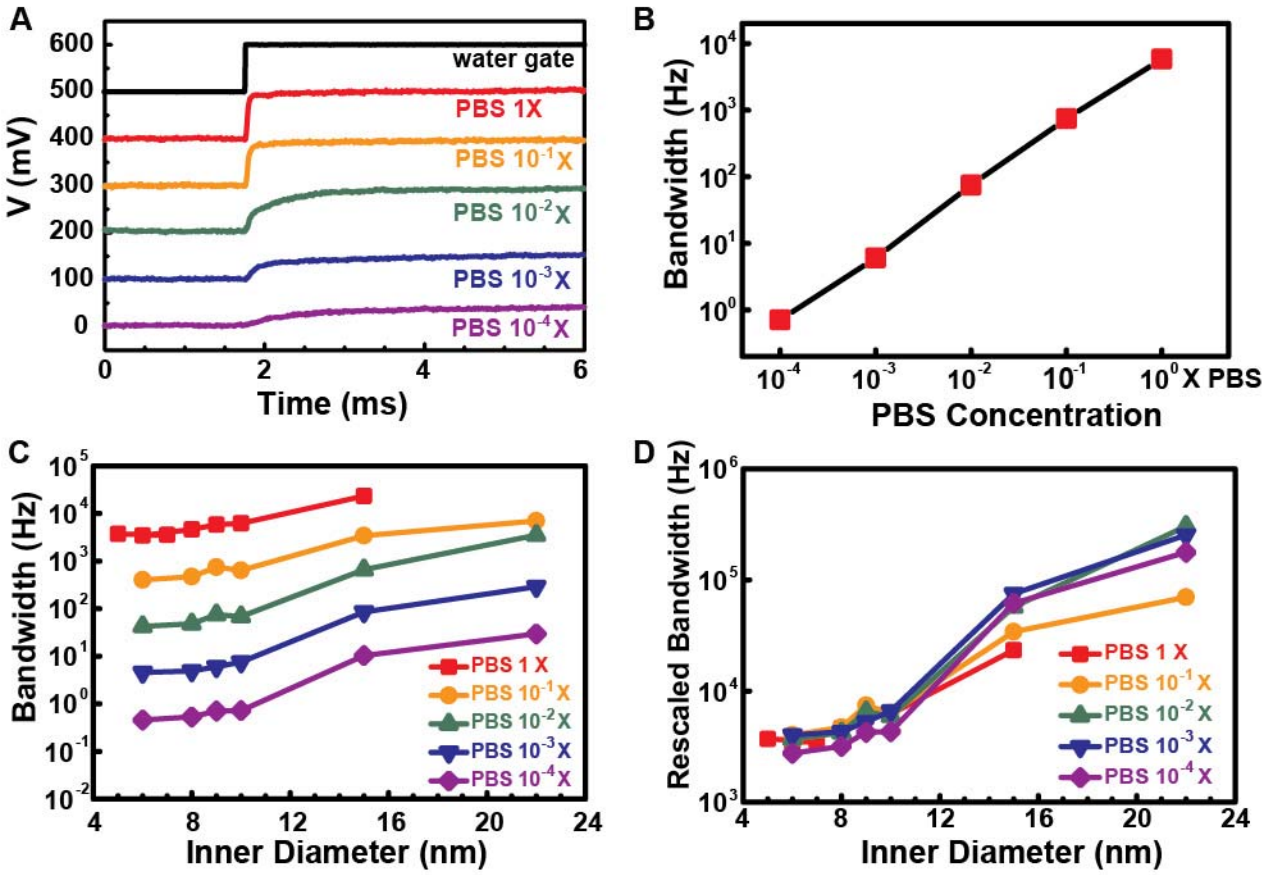
A
V (mV)
Time (ms)
water gate
PBS 1X
PBS 10-1X
PBS 10-2X
PBS 10-3X
PBS 10-4X
B
Bandwidth (Hz)
PBS Concentration
10-4
10-3
10-2
10-1
100 X PBS
C
Bandwidth (Hz)
Inner Diameter (nm)
PBS 1 X
PBS 10-1X
PBS 10-2X
PBS 10-3X
PBS 10-4X
D
Rescaled Bandwidth (Hz)
Inner Diameter (nm)
PBS 1 X
PBS 10-1X
PBS 10-2X
PBS 10-3X
PBS 10-4X

Figure 3

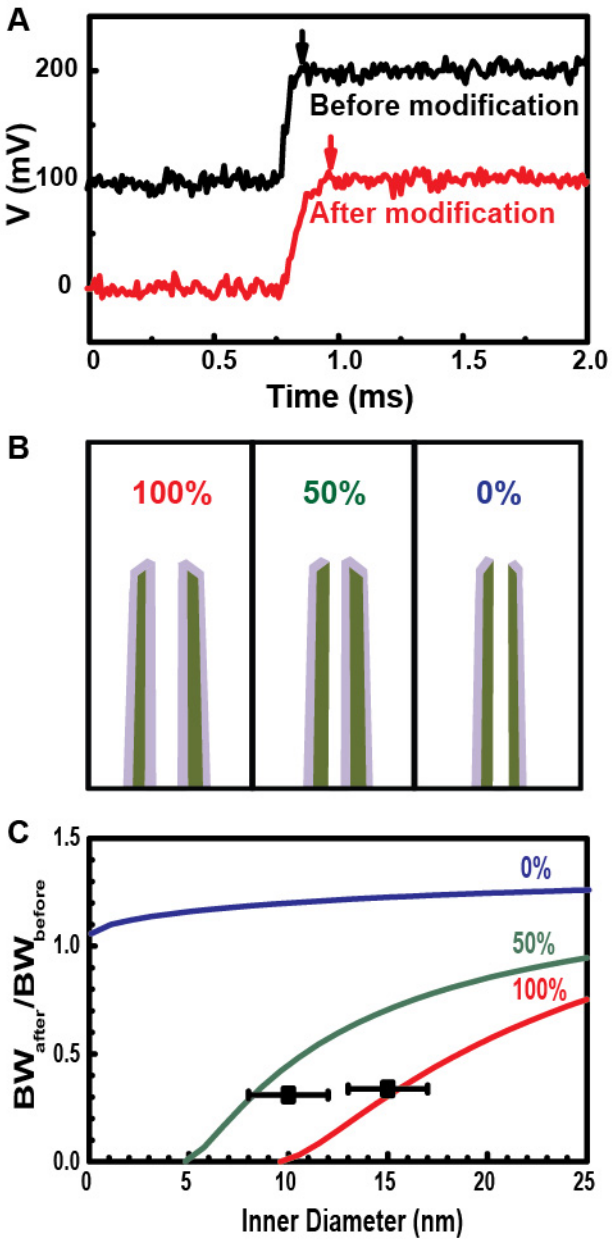
A
200
100
0
V (mV)
Before modification
After modification
0
0.5
1.0
1.5
2.0
Time (ms)
B
100%
50%
0%
C
1.5
1.0
0.5
0.0
BW_after/BW_before
0%
50%
100%
0
5
10
15
20
25
Inner Diameter (nm)

Figure 4

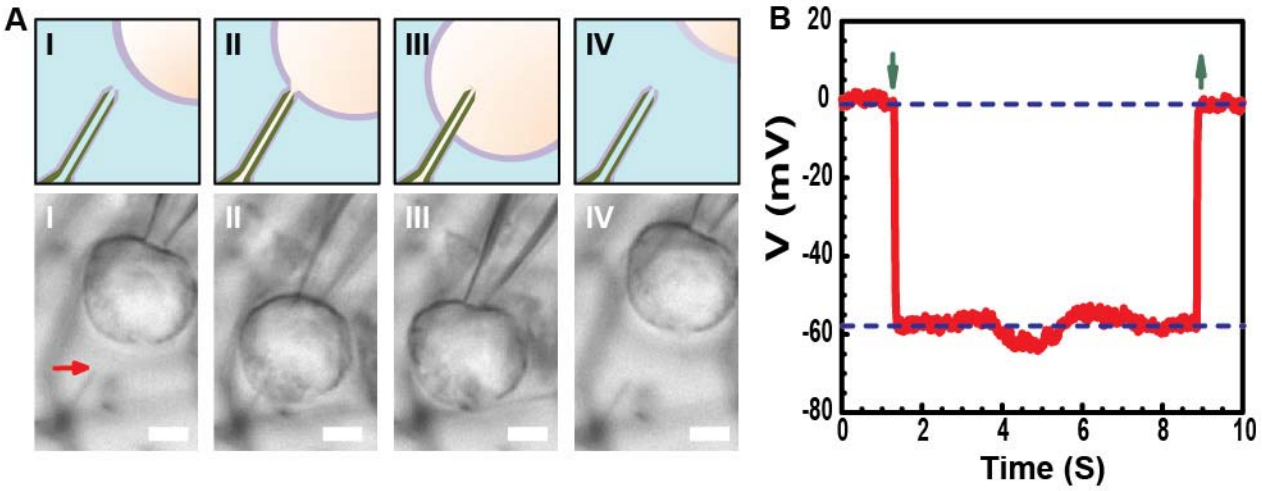

Figure 5

Supporting Information for:

Sub-10 nanometer intracellular bioelectronic probes from nanowire-nanotube heterostructures

Tian-Ming Fu, Xiaojie Duan, Zhe Jiang, Xiaochuan Dai, Ping Xie, Zengguang Cheng, Charles M. Lieber

This PDF file includes:
SI text
Figures Legends S1-S5
Supplementary References

SI text

Silicon nanowire synthesis. Boron-doped p-type silicon nanowires (SiNWs) were synthesized using a gold (Au) nanoparticle catalyzed chemical vapor deposition (CVD) methodology described previously (S1). Briefly, 100 nm diameter Au nanoparticles (Ted Pella, Inc.) were dispersed on an oxidized silicon (Si) wafer (600 nm silicon dioxide (SiO_2), Nova Electronic Materials). Syntheses were carried out at 450-460 °C and 25 torr, with 2.5 standard cubic centimeters per minute (sccm) pure silane (SiH_4) as the silicon source, 3 sccm diborane (B_2H_6) (100 ppm in He) as the boron (B) dopant source and 10 sccm argon (Ar) as the carrier gas. Under these conditions, the resulting SiNWs have diameters of ca.100 nm and a delivered doping ratio of 4000:1 (Si:B). The total growth time was 40 min.

SiNW field-effect transistor (FET) fabrication. SiNWs were suspended in isopropanol solution by gentle sonication (2-3 s, 30 W, Crest Ultrasonics) and then dispersed onto the silicon nitride (Si_3N_4) surface of a Si wafer (100 nm thermal SiO_2, 200 nm Si_3N_4, n-type, 0.005 V·cm, Nova Electronic Materials) with predefined outer electrodes (Ti/Pt/Ti, 5/50/30 nm) and markers (Ti/Pt, 5/50 nm). The dispersed SiNWs were spin-coated (4000 rpm for 40 s, each layer) with resists (MMA (8.5), MAA (EL9) and PMMA (950, C2), MicroChem Corp.), and each layer was baked at 185 °C for 5 min. Electron-beam-lithography (EBL, JEOL-7000F) was used to define source/drain (S/D) contacts on individual SiNWs. The typical width of the contacts was 400 nm and the separation between S/D was 600-800 nm. A step of BHF (Buffered HF Improved, Transene) was carried out to eliminate natural SiO_2 on SiNW before thermal evaporation (Sharon Thermal Evaporator) of Ti contact (140 nm thick). A schematic of SiNW FET fabrication is presented in Fig. S1, panels A, B.

Germanium nanowire synthesis. Germanium nanowires (GeNWs) were grown on top of the resulting SiNW FETs as follows: First, 35 nm thick Au nanodots with ca. 80 nm diameter were defined by EBL and thermal evaporation on top of SiNW FETs between predefined S/D (Fig. S1*C*). Second, the chip was placed in the CVD reactor, and GeNW growth was initiated by nucleation at 315 °C, and 300 torr for 1 min with 20 sccm germane (GeH_4) (10% in hydrogen (H_2)) as the germanium source, 200 sccm H_2 as the carrier gas, followed by elongation step at 285 °C, and 100 torr for 20-40 min (gas flow same as for nucleation). The resulting GeNWs have lengths ca. 3-4 μm and a slight taper with bottom diameters ca. 80-90 nm and top diameters ca. 50-60 nm (Fig. S1*D*).

GeNW diameter reduction. The upper 80% portion of the GeNWs were etched in hydrogen peroxide (H_2O_2) solution to reduce their diameters: (*i*) A diluted photoresist protection layer (Shipley S1805: Thinner Type P=1:1, MicroChem Corp) with a thickness of ca. 20% of GeNW length was spin-coated to cover the bottom part of GeNWs (Fig. S1*E*) and baked at 115 °C for 5min. (*ii*) The chip was then placed in 0.17% H_2O_2 solution at 0 °C, and etched for 2-2.5 min.; the calibrated H_2O_2 etching rate was 10-12 nm/min. (*iii*) After etching, the photoresist layer was removed in acetone (without drying), subsequently transferred to 200-proof ethanol, and dried with critical point dryer (Auto Samdri 815 Series A, Tousimis). The resulting GeNWs had 5-10 nm diameters (controlled by etching time) for the upper 80% portion and 80-90 nm diameters for the lower 20% portion of the GeNWs (Fig. S1*F*).

Nanotube fabrication. To fabricate thin but mechanically robust SiO_2 nanotubes, we combined atomic layer deposition (ALD) and a two-step BHF etching as follows: First, a uniform 30 nm SiO_2 layer, which serves as both the nanotube wall and metal electrode passivation, was conformally deposited by ALD (Savannah-S200, Cambridge NanoTech) at 250 °C (Fig. S1*G*). Second, a photoresist protection layer (~ 20% of GeNW length) was spin-coated and baked (Fig. S1*H*), and then the upper unprotected part of the SiO_2 layer was etched in BHF (Buffered HF Improved, Transene) to ~10 nm (Fig. S1*I*); the etching rate was ~1.5 nm/min and was calibrated. Third, following lift-off of the former protection resist layer, a thicker photoresist layer (Shipley S1813 or S1818, MicroChem Corp.) was spin-coated and baked at 115 °C for 5min as shown in Fig. S1*J*. A second step of BHF etching was used to remove the exposed SiO_2 layer at the GeNW tip; the SiO_2 shell is tapered during this step due to etching along the axial and radial direction (Fig. S1*K*). After photoresist lift-off, the chip was transferred to H_2O_2 solution (30%, Sigma) to etch selectively the Ge (60 °C, 60 min), which produces the nanotube probe, and then the chip was dried in the critical point dryer. The resulting nanotubes have an inner diameter 5-10 nm and 10 nm tapered SiO_2 wall for the upper 80% portion and an inner diameter 80-90 nm and 30 nm SiO_2 wall for the lower 20% part (Fig. S1*L*).

Device electrical characterization. The behavior of the ultra-small BIT-FET devices in aqueous solution was characterized in two distinct ways in order to determine their quasi-static and dynamic responses. (*i*) Standard quasi-static water-gate measurements were carried out in 1x phosphate buffered saline (1x PBS, Mediatech, Inc.) to characterize the device sensitivity as follows: The water-gate potential, V_{wg}, was varied at 50 mV/s (via Ag/AgCl electrode) while monitoring the SiNW FET current for fixed 100 mV S/D voltage; the FET current was amplified

(1211, DL Instruments) and digitized at 100 kHz sampling rate (Axon Digidata 1440A Data Acquisition System, Molecular Devices, Inc.). The resulting current versus V_{wg} curves are used to calibrate the sensitivity (transconductance) for the devices. (*ii*) A quasi-step-function water-gate pulse was used to characterize the bandwidth (BW) of the ultra-small BIT-FET devices in different concentration PBS solutions. In short, a 0.01 ms rise-time 100 mV amplitude V_{wg} step was applied (Axon Digidata 1440A Data Acquisition System, Molecular Devices, Inc.) while simultaneously recording the corresponding current variation of the ultra-small BIT-FET, which was amplified, filtered at 30 kHz (CyberAmp 380, Molecular Devices, Inc.), and then digitized at a 100 kHz sampling rate. A 100 mV DC source voltage was used in all of the measurements.

Device bandwidth model. The calculation of the ultra-small BIT-FET bandwidth is based on the model described for conventional BIT-FETs in (S1), and the equivalent circuit is shown in Fig. S5*A*. With a applied step water-gate pulse (i.e. $V_{out} = V_0\theta(t)$ with V_0 being the pulse amplitude and $\theta(t)$ is the step function equals 1 for $t > 0$ and 0 for $t < 0$), this circuit can be described by the following partial differential equation,

$$\frac{\partial^2 V_{in}}{\partial z^2} = \rho_R \rho_C \left(\frac{\partial V_{in}}{\partial t} - \frac{\partial V_{out}}{\partial t} \right) = \rho_R \rho_C \left(\frac{\partial V_{in}}{\partial t} - V_0 \delta(t) \right) \tag{3}$$

where V_{in}, V_{out}, ρ_R, ρ_C, z and t correspond to the potential inside the ultra-small nanotube, the potential outside the nanotube, the linear resistivity of the solution inside the tube, the capacitance of the ultra-small nanotube wall per unit length, the distance from the nanotube opening, and time, respectively.

For numerical simulations (Model 1 and 2 in Fig. 2*D*), we used a 1D finite element method to evaluate the potential change at the end of the SiO_2 nanotube as a function of time following equation (3). We fixed the length of SiO_2 nanotube L=2.5 μm and the thickness as d=10 nm. Two models corresponding to the upper and lower bandwidth limits were considered. In model 1, the active channel is limited to the area defined by the GeNW base, and in model 2, the active channel corresponds to the entire active SiNW surface. These two models represented the scenarios of no Ge overcoating and complete Ge overcoating (we use a 10 nm Ge overcoating thickness based on experimental data; this Ge is removed during GeNW etching to produce the larger active area), respectively, on the SiNW.

Previous simulation results (S1) revealed that the device bandwidth is mainly limited by the small diameter nanotube, and thus, that the tip access impedance and capacitive coupling to underlying SiNW FET can be ignored. We used these simplifications and the initial condition of $V_{in}(z,0)=0$, we used the Laplace transform to obtain an analytical solution for equation (3) as,

$$\frac{V_{in}}{V_0} = \frac{1}{\sqrt{\pi}} \int_0^{\frac{4t}{\rho_R \rho_C z^2}} \frac{\exp(-\frac{1}{x})}{x^{3/2}} dx \tag{4}$$

Since bandwidth (BW) is inversely proportional to the time needed for $\frac{V_{in}}{V_0}$ to increase from 0.1 to 0.9, we obtain

$$BW \propto \frac{1}{t_{0.9} - t_{0.1}} \propto \frac{1}{\rho_R \rho_C L^2} \propto \frac{\ln(1 + \frac{2t_{SiO_2}}{d}) d^2}{\rho_{sol} L^2} \tag{5}$$

where ρ_R, ρ_C , d, t_{SiO_2}, L, ρ_{sol} are the solution linear resistivity, effective nanotube wall capacitance per unit length, nanotube inner diameter, nanotube thickness, nanotube length and

liquid resistivity, respectively. Based on this relation, we can rescale measured bandwidth results by nanotube diameter, length or liquid resistivity (conductivity).

Effect of phospholipid modification on device bandwidth. From equation (5), we can estimate the effect of phospholipid modification on device bandwidth by considering the change of ρ_R and ρ_C. For example, if phospholipid bilayers modify both inner and outer surfaces of the tube, ρ_R increases to $\left(\frac{d}{d-2t_{lipid}}\right)^2 \rho_R$ resulting from the reduction of the effective nanotube inner diameter and ρ_C decreases to $\frac{\rho_C}{1+\frac{\varepsilon_{r_{SiO_2}}}{\varepsilon_{r_{lipid}}}\frac{\ln(\frac{d}{d-2t_{lipid}})+\ln[\frac{d+2(t_{SiO_2}+t_{lipid})}{d+2t_{SiO_2}}]}{\ln(\frac{d+2t_{SiO_2}}{d})}}$ since the lipid bilayers act as new capacitors connected with the nanotube wall capacitor in series. Here, t_{lipid}, $\varepsilon_{r_{SiO_2}}$ and $\varepsilon_{r_{lipid}}$ are double layer phospholipid thickness (ca. 4.75 nm (S2)), relative dielectric constant of SiO_2 (ca. 3.9 (S3)) and relative dielectric constant of bilayer phospholipid (ca. 5 (S4)). From equation (5), the ratio of the bandwidth after to before modification can be expressed as

$$\frac{BW_{after}}{BW_{before}} = \frac{(d-2t_{lipid})^2}{d^2}\left\{1+\frac{\varepsilon_{r_{SiO_2}}}{\varepsilon_{r_{lipid}}}\frac{\ln(\frac{d}{d-2t_{lipid}})+\ln[\frac{d+2(t_{SiO_2}+t_{lipid})}{d+2t_{SiO_2}}]}{\ln(\frac{d+2t_{SiO_2}}{d})}\right\} \quad (6)$$

This ratio versus nanotube inner diameter is plotted in Fig. 4*C* (100%, red line) of the main text. Similarly, we obtain expressions for bandwidth ratio for the cases where the inner surface is only half covered and not covered at all. The nanotube inner diameter dependence of these ratios is plotted in Fig. 4*C* (50%, green line and 0%, blue line).

Supplementary Figure Legends:

Fig. S1. Schematics of the fabrication flow for the ultra-small BIT-FET. (*A*) SiNWs (blue) are dispersed on substrate (solid gray). (*B*) S/D contacts are defined by EBL followed by thermal evaporation. (*C*) Au nanodots are defined on SiNWs between S/D using EBL and thermal evaporation. (*D*) GeNWs (red) are grown on top of the SiNWs through nanocluster-catalyzed CVD process. (*E*) A thin layer of photoresist (transparent gray) is spin-coated on the chip to protect the lower GeNW part. (*F*) The resulting H_2O_2 etched GeNWs following photoresist lift-off. Only the GeNW above the photoresist in (*E*) is thinned by etching in H_2O_2. (*G*) SiO_2 is conformally deposited over the entire chip by ALD. (*H*) A thin layer of photoresist (transparent gray) is spin-coated to protect the lower region of chip. (*I*) The resulting BHF etched structures following lift-off. The region of SiO_2 above the photoresist layer in (*H*) is etched to ca.10 nm thickness. (*J*) Photoresist with thickness smaller than the GeNW heights is deposited. (*K*) The resulted structure following BHF etching of SiO_2, which exposes the tips of the GeNWs. Isotopic BHF etching yields a small taper with thinner SiO_2 at the topmost part of the structure. (*L*) The GeNW is removed by H_2O_2 etching to form an ultra-small nanotube connected to the bottom SiNW FET.

Fig. S2. Electron microscopy characterization of the ultra-small BIT-FET. (*A*) Representative scanning electronic microscope (SEM) (Zeiss Ultra Plus field-emission SEM) images of intermediate fabrication steps of the ultra-small BIT-FET. *Left*: Device after 30 nm ALD coating of SiO_2. *Right*: Device after first step of selective BHF etching of the upper 80% portion of the SiO_2 to ca. 10 nm (Fig. S1 *H* and *I*). White dashed lines in *I* and *II* indicate the point below which the SiO_2 is protected by photoresist during BHF etching. Scale bars: 200

nm. (*B*) False colored transmission electron microscopy (JEOL 2100 TEM) image of an ultra-small nanotube. This tube was fabricated following the same procedure as described in SI text, and deposited onto lacey carbon grids (Ted Pella) from ethanol suspension. It has a tip ID ~7 nm, and bottom ID ~ 80 nm. False color is used here to distinguish the SiO_2 nanotube from background amorphous carbon. Scale bar: 50 nm.

Fig. S3. Sensitivity of different device structures. (*A*), (*B*) Schematics of the ultra-small BIT-FET without and with Ge overcoating on the SiNW, respectively. Panels (*I*) and (*II*) correspond to the BIT-FET devices before and after Ge core etching. Panels (*III*) show schematically typical conductance (G) vs. water-gate (V_{wg}) measurements from these distinct structures.

Fig. S4. Dynamic water-gate responses from ultra-small BIT-FETs. (*A*) Pulsed (i.e., step function) V_{wg} and corresponding conductance (G) vs. time responses from a 10 nm ID ultra-small BIT-FET in different concentration PBS solutions. The applied V_{wg} with a 100 mV amplitude pulses had rise/fall times of 100, 10, 0.3 and 0.05 ms in (*I*), (*II*), (*III*) and (*IV*), respectively. The duration of the pulse is ten times the rise/fall time in all measurements. The peak and dip features associating with the rise and fall of the water-gate pulse is due to the capacitive coupling to passivated metal electrodes (S1). Red arrows indicate the PBS solution concentration at which the ultra-small BIT-FET response can no longer respond to the applied water-gate pulse without time delay. (*B*) Removal of capacitive signals from the passivated metal electrodes. A 100 mV pulsed water-gate V_{wg} with 0.3 ms rise/fall time was applied (*I*). Experimental responses from both ultra-small BIT-FET and passivated metal electrodes (*II*), and only the passivated metal

electrodes (i.e., V(S/D) = 0) (*III*) are shown. Subtraction of (*III*) from (*II*) yields the pure field effect response from the ultra-small BIT-FET (*IV*).

Fig. S5. Device bandwidth circuit model. Equivalent circuit for the device bandwidth modeling of the BIT-FET.

Supplementary References:

S1. Duan XJ, et al. (2012) Intracellular recordings of action potentials by an extracellular nanoscale field-effect transistor. Nat Nanotechnol 7(3):174-179.

S2. Stern HA & Feller SE (2003) Calculation of the dielectric permittivity profile for a nonuniform system: Application to a lipid bilayer simulation. J Chem Phys 118(7):3401-3412.

S3. Gray PR (2009) Analysis and design of analog integrated circuits (Wiley, New York) 5th Ed pp xiv, 881 p.

S4. Weaver JC & Schoenbach KH (2003) Biodielectrics. IEEE T Dielect El In 10(5):715-716.

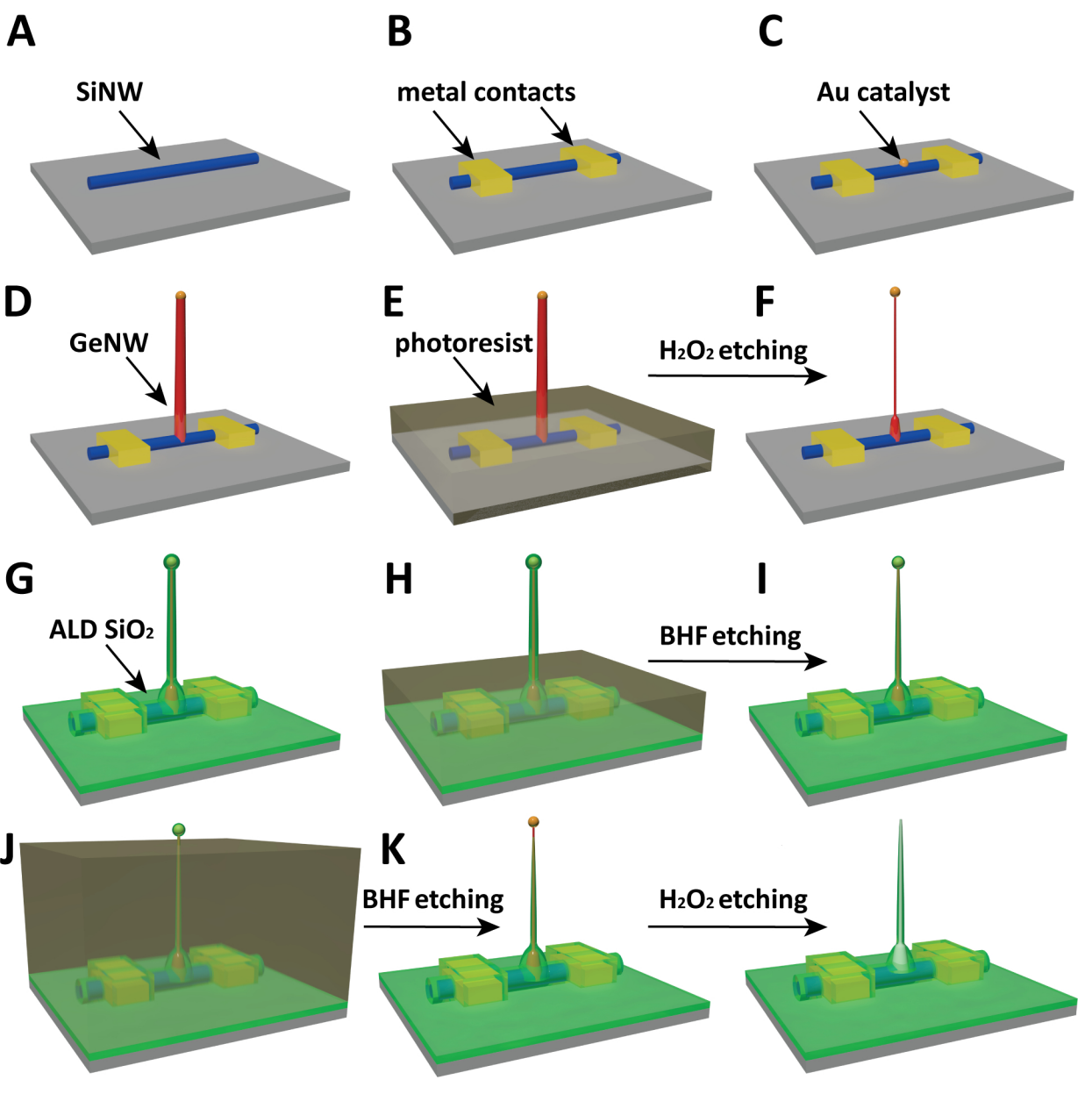
A
SiNW
B
metal contacts
C
Au catalyst
D
GeNW
E
photoresist
F
H2O2 etching
G
ALD SiO2
H
I
BHF etching
J
K
BHF etching
H2O2 etching

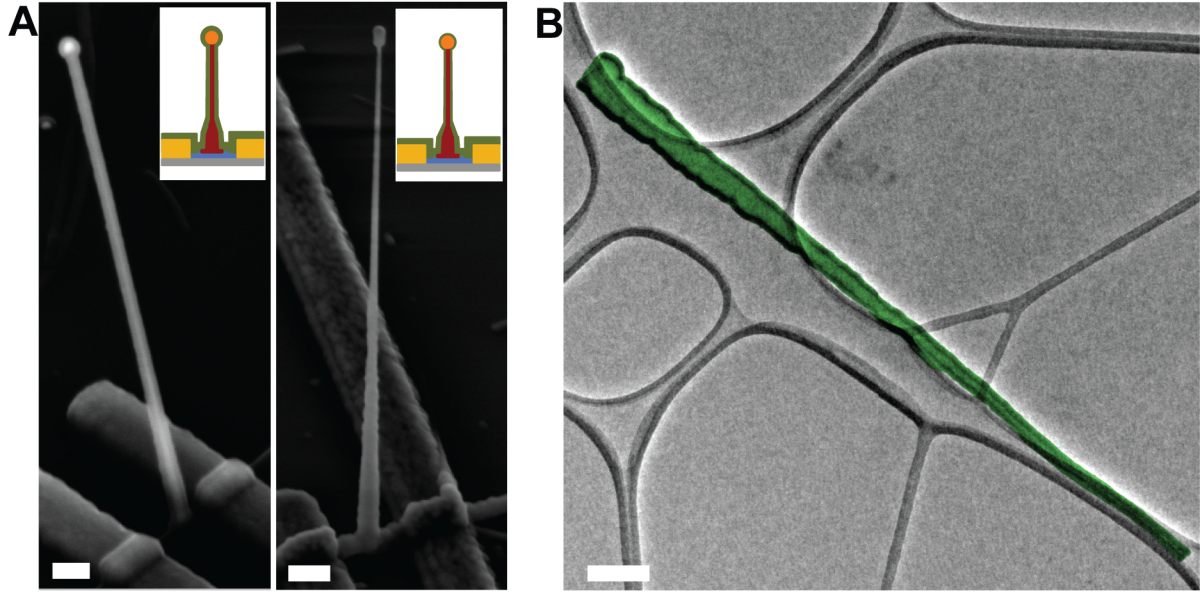
A
B

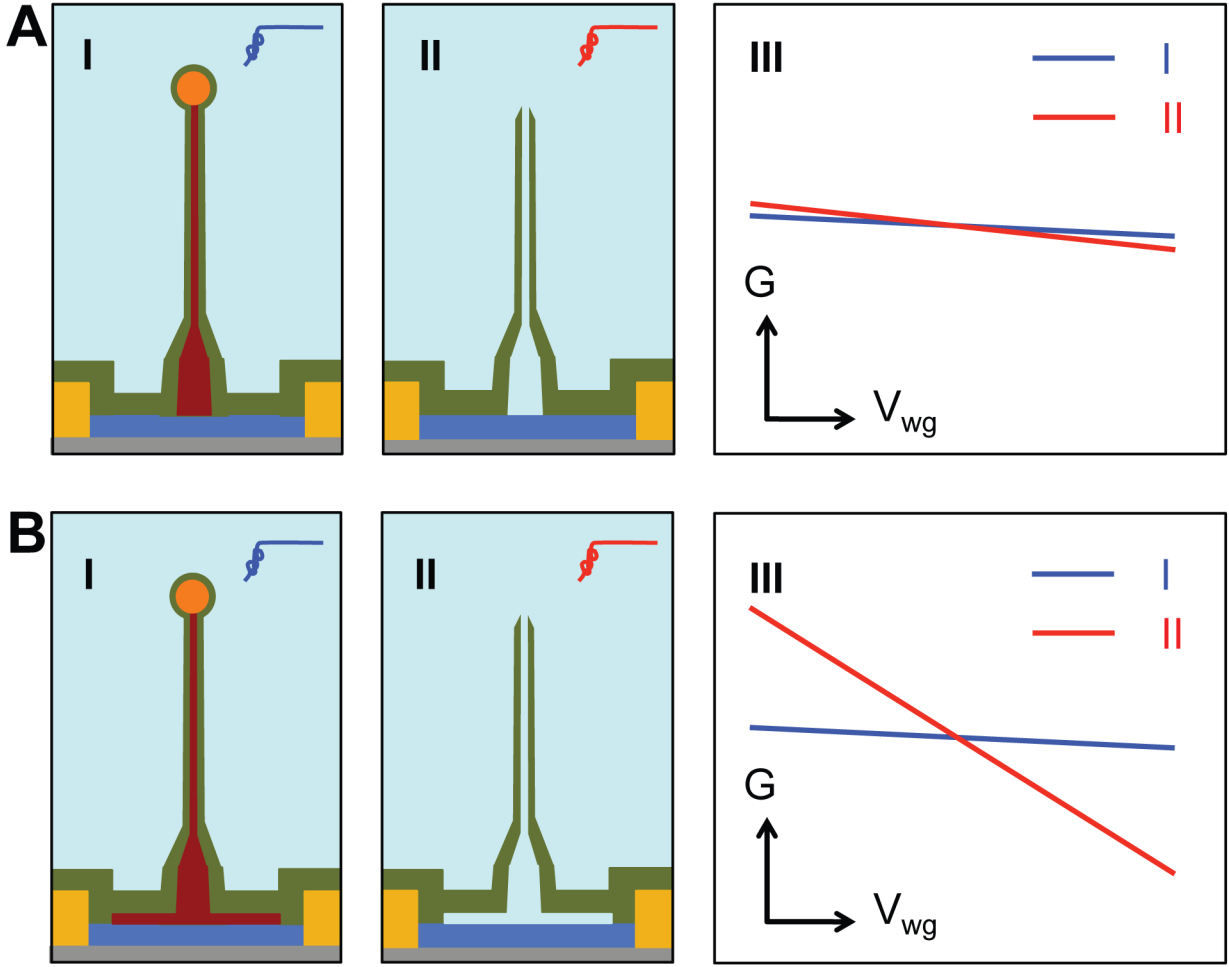
A
I
II
III
I
II
G
V_{wg}
B
I
II
III
I
II
G
V_{wg}

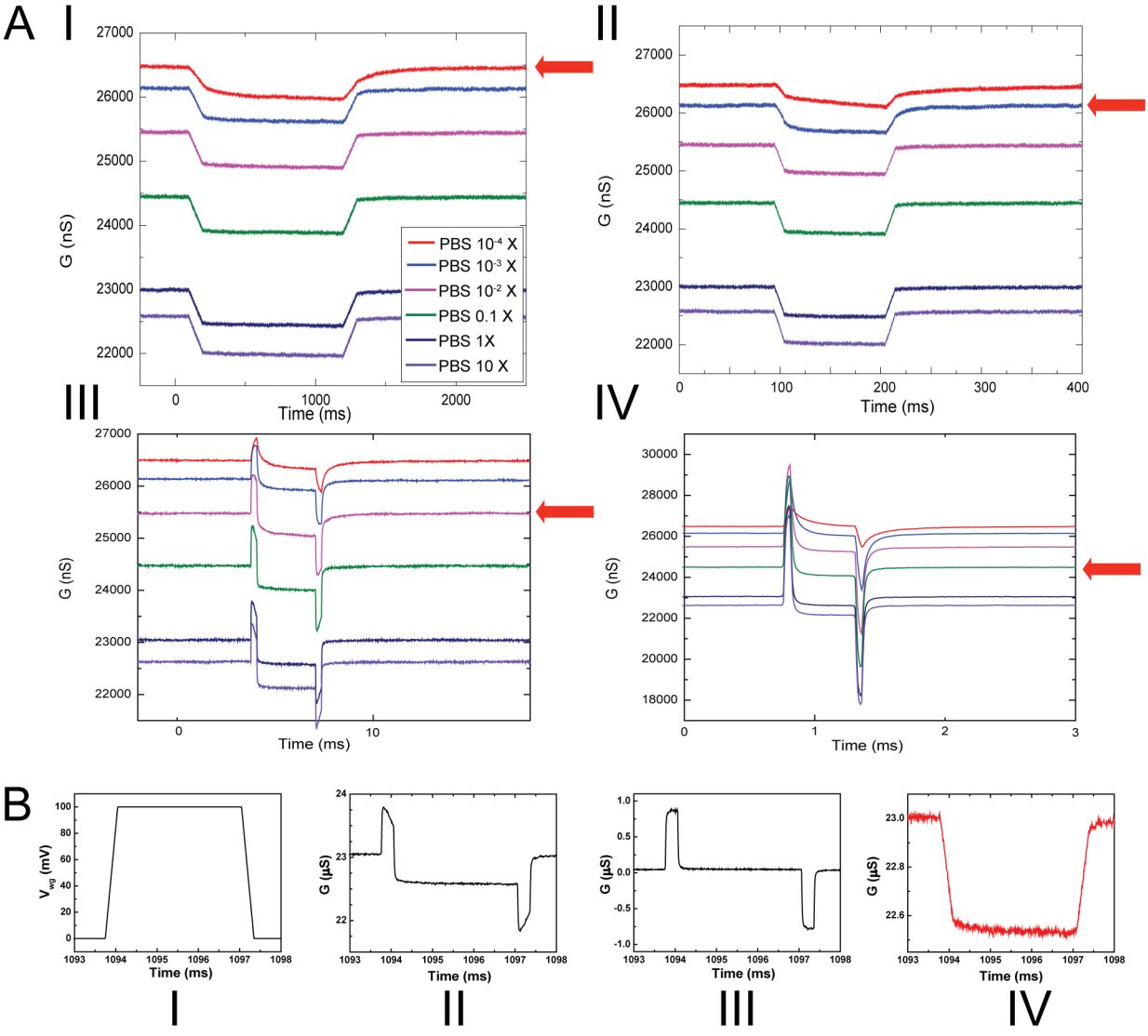
A
I
II
III
IV
G (nS)
Time (ms)
PBS 10-4 X
PBS 10-3 X
PBS 10-2 X
PBS 0.1 X
PBS 1X
PBS 10 X
B
Vwg (mV)
G (μS)
Time (ms)
I
II
III
IV

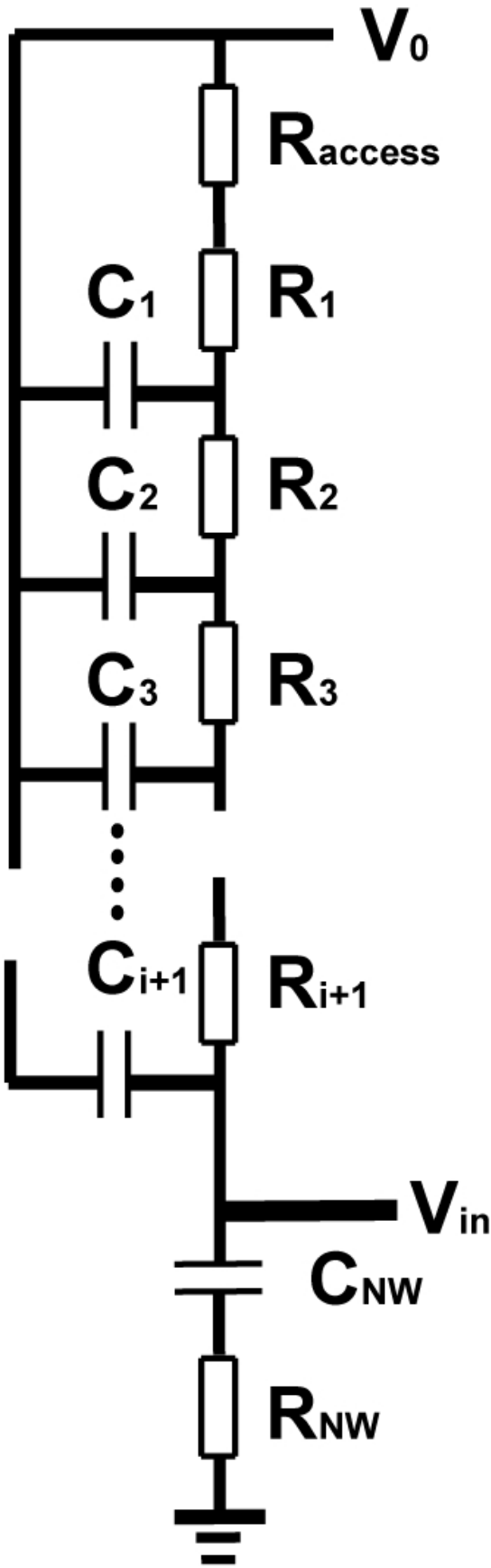
V0
Raccess
C1
R1
C2
R2
C3
R3
Ci+1
Ri+1
Vin
CNW
RNW